1   **Aerosol hygroscopicity over the South-East Atlantic Ocean during the**

2   **biomass burning season: Part I – From the perspective of scattering**

3   **enhancement**

4   **Lu Zhang[1,2], Michal Segal-Rozenhaimer[1,3,4*], Haochi Che[2*], Caroline Dang[3,4], Junying**

5   **Sun[5], Ye Kuang[6,7], Paola Formenti[8], Steven G. Howell[9]**

6   [1]Department of Geophysics, Porter School of the Environment and Earth Sciences, Tel Aviv

7   University, Tel Aviv, Israel

8   [2]Department of Geosciences, University of Oslo, Oslo, Norway

9   [3]Bay Area Environmental Research Institute, Moffett Field, California, USA

10   [4]NASA Ames Research Center, Moffett Field, California, USA

11   [5]State Key Laboratory of Severe Weather & Key Laboratory of Atmospheric Chemistry,

12   Chinese Academy of Meteorological Sciences, Beijing, China

13   [6]Institute for Environmental and Climate Research, Jinan University, Guangzhou, China

14   [7]Guangdong-Hongkong-Macau Joint Laboratory of Collaborative Innovation for

15   Environmental Quality, Guangzhou, China

16   [8]Université Paris Cité and Univ Paris Est Creteil, CNRS, LISA, Paris, France

17   [9]Department of Oceanography, University of Hawai'i at Mānoa, Honolulu, USA

18   Correspondence: Michal Segal-Rozenhaimer (msegalro@tauex.tau.ac.il) and Haochi Che

19   (haochi.che@geo.uio.no)

20 **Abstract**

21 Aerosol hygroscopicity plays a vital role in aerosol radiative forcing. One key parameter

22 describing hygroscopicity is the scattering enhancement factor, f(RH), defined as the ratio of

23 the scattering coefficient at humidified relative humidity (RH) to its dry value. Here, we utilize

24 the f(80%) from ORACLES 2016 and 2018 airborne measurements to investigate the

25 hygroscopicity of aerosols, its vertical distribution, its relationship with chemical composition,

26 and its sensitivity to organic aerosol (OA) hygroscopicity over the South-East Atlantic (SEA)

27 Ocean during the biomass burning (BB) season.

28 We found that aerosol hygroscopicity remains steady above 2 km, with a mean f(80%) of

29 1.40±0.17. Below 2 km, aerosol hygroscopicity increases with decreasing altitude, with a mean

30 f(80%) of 1.51±0.22, consistent with higher values of BB hygroscopicity found in the literature.

31 The hygroscopicity parameter of OA (κ_{OA}) is retrieved from the Mie model with a mean value

32 of 0.11±0.08, which is in the middle to upper range compared to literature. Higher OA

33 hygroscopicity is related to aerosols that are more aged, oxidized, and present at lower altitudes.

34 The enhanced BBA hygroscopicity at lower altitudes is mainly due to a lower OA fraction,

35 increased sulphate fraction, and greater κ_{OA} at lower altitudes.

36 We propose a parameterization that quantifies f(RH) with chemical composition and κ_{OA} based

37 on Mie simulation of internally mixed OA-$(NH_4)_2SO_4$-BC mixture. The good agreement

38 between the predictions and the ORACLES measurements implies that the aerosols in the SEA

39 during the BB season can be largely represented by the OA-$(NH_4)_2SO_4$-BC internal mixture

40 with respect to the f(RH) prediction. The sensitivity of f(RH) to κ_{OA} indicates that applying a

41 constant κ_{OA} is only suitable when the OA fraction is low and κ_{OA} shows limited variation.

42 However, in situations deviating these two criteria, κ_{OA} can notably impact scattering

43   coefficients and aerosol radiative effect; therefore, accounting for κ_{OA} variability is

44   recommended.

45   **Keywords:** hygroscopicity, biomass burning aerosol, chemical composition, κ_{OA}, Atlantic,

46   airborne measurements, parameterization

47

1 Introduction

Aerosol hygroscopicity is an important physicochemical property of atmospheric aerosols, representing the extent to which particles take up water when exposed to a certain relative humidity (RH) (Covert et al., 1972). Key parameters describing aerosol hygroscopicity include the scattering enhancement factor, f(RH), which represents the enhancement of the aerosol light-scattering coefficient as a function of RH (Carrico et al., 2003), and κ, the hygroscopicity parameter, whose value is defined by its effect on the water activity of the solution (Petters and Kreidenweis, 2007). Water uptake will increase the size and the mass of hygroscopic aerosols, alter their refractive index, enhance the scattering ability, and ultimately influence the single scattering albedo and aerosol radiative forcing (Cotterell et al., 2017; Titos et al., 2021; Zieger et al., 2013). Furthermore, hygroscopicity affects aerosols' ability to act as CCN (cloud condensation nuclei) and ice nuclei, and further influences cloud properties and precipitation (Cai et al., 2021; Che et al., 2017; Ervens et al., 2007). Model results show that even a modest change in κ_{OA} (κ of organic aerosols) can lead to significant changes in CCN, droplet number concentration, and aerosol radiative effects (Liu and Wang, 2010; Rastak et al., 2017). The treatment of aerosol hygroscopicity is one of the key factors contributing to discrepancies between model simulations and observations and among model estimates (Burgos et al., 2020; Haywood et al., 2008; Reddington et al., 2019).

Africa emits ~ 1/3 of the Earth's annual BB emissions (van der Werf et al., 2010), and its burned areas are increasing every year (Andela et al., 2017). Every Austral spring (July to October), the BB aerosols (BBAs) from African fires are transported westward through the free troposphere (FT) over the persistent stratocumulus cloud deck in the South-East Atlantic (SEA), and eventually subside into the marine boundary layer (MBL) (Redemann et al., 2021). BBAs undergo atmospheric processing during transport, altering their chemical composition, oxidation extent, particle polarity, molecular weight, volatility, and solubility (Rastak et al.,

73   2017), making the hygroscopicity highly variable. Laboratory studies show that minutes-old

74   BBAs are more hygroscopic than hour-old BBAs (Day et al., 2006), while the hygroscopicity

75   of BBAs transported for more than several days in the SEA region remains an area of

76   investigation. Furthermore, these BBAs mix with pristine aerosols and are subject to marine

77   influences from the SEA, resulting in a distinct vertical variation of aerosol hygroscopicity.

78   The hygroscopicity of organic aerosol (OA), the dominant component of aerosols in

79   most cases, is poorly characterized due to its chemical complexity (Kuang et al., 2020; Mei et

80   al., 2013). Values of κ_{OA} can range from 0 for hydrophobic freshly emitted organics to >1.0 for

81   very hygroscopic amino acids (Kuang et al., 2020; Petters et al., 2009; Zhang et al., 2007).

82   BBOA is usually regarded as hydrophobic, while the mass fraction of aged BBOA shows a

83   positive correlation with κ_{OA} (Cerully et al., 2015; Kuang et al., 2021). Several studies have

84   found a linear correlation between OA hygroscopicity and its oxidation level, commonly

85   characterized by the oxygen-to-carbon (O/C) ratio or the fraction of total organic mass spectral

86   signal at m/z 44 (f_{44}) (Lambe et al., 2011; Mei et al., 2013). However, this linear relationship

87   is not always established, especially for secondary OA with a lower O/C ratio under sub-

88   saturated conditions, for which solubility may play a more important role. In addition, studies

89   show molecular weight, surface tension, and liquid-liquid phase separation are also related to

90   the water affinity of OA (Liu et al., 2018; Rastak et al., 2017; Wang et al., 2019), all

91   contributing to the complexity of OA hygroscopicity.

92   The ORACLES (ObseRvations of Aerosols above CLouds and their intEractionS)

93   campaign (Redemann et al., 2021) provides a comprehensive observation of aerosols above the

94   SEA Ocean with 4-12 days of transport from Africa fires, making it a valuable opportunity to

95   investigate the hygroscopicity of aged BBA and their OA. In this paper, we first characterize

96   the aerosol hygroscopicity and its vertical distribution over the SEA during the BB season, then

97   propose a parameterization relating aerosol hygroscopicity with chemical composition and k_{OA},

5

98 and evaluate the sensitivity of aerosol hygroscopicity to k_{OA}. Results are expected to provide a

99 reference to the treatment of aerosol hygroscopicity in climate models and satellite retrievals,

100 and to contribute to aerosol-cloud-interactions and radiative assessments in this climatically

101 important SEA region.

102 **2 Methods**

103 2.1 Aircraft Instrumentation and Data Analysis
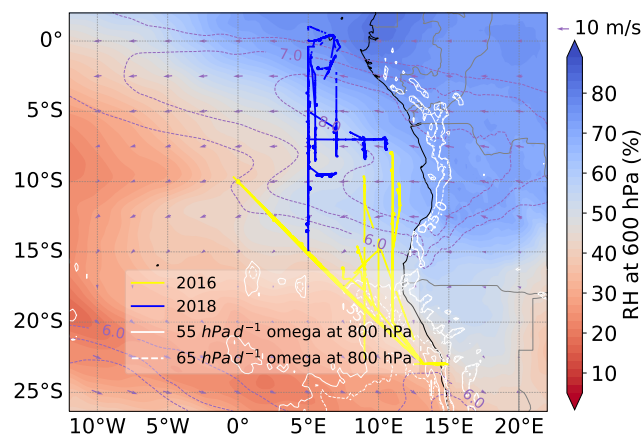
104

105 Figure 1. Flight tracks in 2016 and 2018 ORACLES campaigns. Map of October mean of

106 ERA5 600 hPa RH overlaid by the 600 hPa zonal wind (purple contours; 6, 7, and 8 m s^{-1}),

107 600 hPa horizontal wind vector (purple arrows; m s^{-1}), and ORACLES flight tracks in 2016

108 (yellow) and 2018 (blue), respectively. White contours are the 2016 September mean vertical

109 velocity, omega, at 800 hPa. Solid and dashed lines represent the subsidence of 55 and 65

110 hectopascals per day (hPa d^{-1}).

111 We analyzed airborne, in situ data measured over the SEA region from the ORACLES

112 campaign performed in September 2016 and October 2018 (Redemann et al., 2021). The flight

113 tracks are shown in Fig. 1. All instruments were deployed on the NASA P-3 aircraft. Two

114 Radiance Research (RR) M903 integrating nephelometers (Nephs) were operating in parallel,

115   one (referred to as the 'reference Neph') under relatively dry conditions and the other (known

116   as the 'humidified Neph') maintained at ~80 % RH. Temperature errors are about 0.5℃ and

117   RH errors are roughly 3 %. Measurements were reported at 1 Hz. Particles entering the

118   reference Neph were heated to the aircraft cabin temperature, which significantly reduced their

119   RH in the Neph. For the calculation of f(RH), data with reference Neph RH > 30 % were

120   excluded. Calibrations were performed in the field with refrigerant R-134A (1,1,1,2-

121   tetrafluoroethane). All scattering coefficients and scattering enhancement factors are reported

122   at 540 nm wavelength.

123   The non-refractory submicron aerosol composition was provided by a High-Resolution

124   Time-of-Flight Aerosol Mass Spectrometer (HR-ToF-AMS, Aerodyne Research Inc.) (Che et

125   al., 2022a). The fragment analysis provided f_{44} and f_{60}, representing the fractions of the OA

126   mass spectrum signals at m/z=44 (mainly CO_2^+) and m/z=60 (mainly $C_2H_4O_2^+$), respectively,

127   in the total OA mass. The mass concentration of refractory BC was provided by a single particle

128   soot photometer (SP2, Droplet Measurement Technology).

129   The dry particle number size distribution (PNSD) with volume equivalent diameter

130   ranging from ~90 nm to 10 μm was obtained by combining measurements from an ultra-high-

131   sensitivity aerosol spectrometer (UHSAS) and an aerodynamic particle sizer (APS). The

132   UHSAS undersized particles and the data were corrected using Howell et al. (2021). The

133   aerodynamic diameter of APS was converted to the volume equivalent diameter according to

134   DeCarlo et al. (2004). Particles were assumed to be spherical (shape factor = 1) with a density

135   of 1.5 g cm^{-3}. The aerosol/plume age was modelled with a two-week forecast using the Weather

136   Research and Aerosol Aware Microphysics (WRF-AAM) model (Thompson and Eidhammer,

137   2014). Carbon monoxide was tagged as tracer at the fire source, identified by a burned area

138   product from the moderate resolution imaging spectrometer with a 500 m spatial resolution.

139   All measurements are averaged to 15 s and adjusted to STP conditions at 273.15 K and

140   1013 hPa. Data with scattering coefficient < 10 Mm^{-1} are not included. f(RH) with RH>30 %

141   for the reference Neph or RH<76 % for humidified Neph are also excluded. The final

142   measurements used in this study have an average RH of 79±0.5 % for the humidified Neph and

143   RH<30 % for the reference Neph. To ensure the influence of BB emissions, only data with

144   f_{60}>0.003 are considered (Cubison et al., 2011). This study analyzes measurements from 21

145   flights totaling approximately 134 flight hours.

146   2.2 Calculation of f(RH) and γ parameterization

147   The aerosol scattering enhancement factor, f(RH), is calculated as:

$$f(RH) = \frac{\sigma_{sp}(RH)}{\sigma_{sp}(RH_{ref})} \qquad (1)$$

148   where σ_{sp}(RH) and σ_{sp}(RH$_{ref}$) represent the scattering coefficients at humidified and reference

149   RHs, respectively. Note the f(RH) only include those with reference RHs equal to or smaller

150   than 30 % to facilitate comparison with previous studies. For simplicity, we denote the f(RH)

151   at the RH of humidified Neph as f(80%), despite the small variation of the RH in humidified

152   Neph. The f(RH) is usually fitted to a γ parameterization to apply to a more extensive RH range

153   (Sheridan et al., 2002; Titos et al., 2016):

$$f(RH) = (\frac{1 - RH/100}{1 - RH_{ref}/100})^{-\gamma} \qquad (2)$$

154   In our case, the γ was calculated with the RH and RH$_{ref}$ using Eq. 2 since the f(RH) was only

155   measured at a fixed RH.

156   2.3 $\kappa_{f(RH)}$ retrieval and κ_{OA} calculation

157   The aerosol hygroscopicity parameter κ can be retrieved from f(RH), usually denoted

158   as $\kappa_{f(RH)}$ (Chen et al., 2014). It can be regarded as the scattering coefficient weighted average κ

159   (Kuang et al., 2021). The dry scattering coefficient can be computed using Mie theory. The

160   Python package PyMieScatt (Sumlin et al., 2018), an implementation of the Mie theory (Mie,

161   1908), was applied in this study. Inputs of the Mie model include particle refractive index and

162   PNSD. Particles beyond PM_1 (particulate matter with an aerodynamic diameter less than 1 μm)

163   are not included in this calculation, which can be supported by their small contribution to the

164   total volume (average < 3 %). By combining Mie model with the κ-Köhler theory, we can then

165   calculate the scattering coefficients under humidified RH conditions. Subsequently, f(RH) and

166   γ can be obtained using Eq. 1 and 2. In the calculation, a volume mixing rule was used to

167   calculate the refractive index under both dry and humidified conditions. The volume of

168   inorganic salts was converted from those of SO_4^{2-}, NO_3^-, and NH_4^+ from AMS following a

169   modified ion-pairing scheme (Gysel et al., 2007; Zhang et al., 2022). The hygroscopic

170   parameter κ and density can be found in Table S1. We iteratively adjust $\kappa_{f(RH)}$ to minimize the

171   difference between the calculated and measured f(RH). Detailed descriptions of the retrieval

172   procedure of $\kappa_{f(RH)}$ can be found in Chen et al. (2014).

173   According to Petters and Kreidenweis (Petters and Kreidenweis, 2007), the overall κ_{chem}

174   can also be calculated from various chemical compositions following the ZSR (Zdanovskii-

175   Stokes-Robinso) mixing rule. Kuang et al. (2020b) thoroughly outlined in Section 3.3 that the

176    $\kappa_{f(RH)}$ can accurately represent the κ_{chem} of PM_1. Therefore, the hygroscopicity parameter of OA,

177   κ_{OA}, can be calculated as:

$$\kappa_{OA} = \frac{\kappa_{f(RH)} - (\sum_{inorg} \kappa_i \varepsilon_i + \kappa_{BC} \varepsilon_{BC} + \kappa_X \varepsilon_X)}{\varepsilon_{OA}}, \qquad (3)$$

178   where *inorg* represents inorganic salts. ε represents the volume fraction of each component.

179   **3 Results and discussion**

180   3.1 Overview of chemical compositions in 2016 and 2018 ORACLES
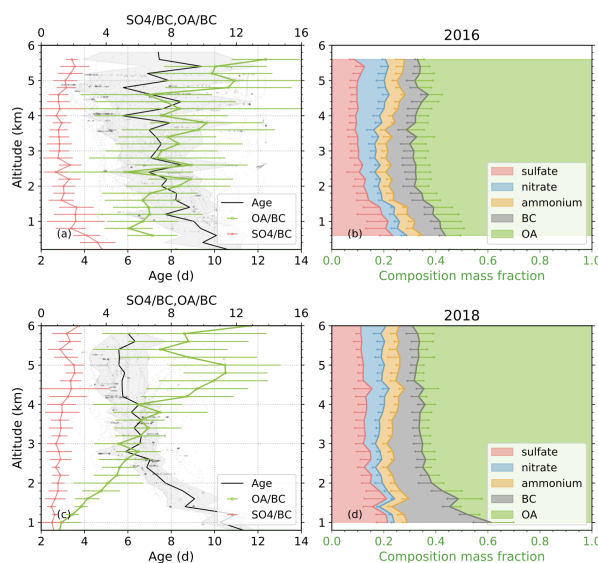
Figure 2. The vertical distribution of plume age and chemical composition. (a, c) Variation of plume age (black), OA/BC, and SO4/BC with altitude in 2016 (upper) and 2018 (lower) ORACLES campaigns, respectively. Grey dots show the distribution of plume age with the altitude. (b, d) The average vertical distribution of the mass ratio of chemical compositions from AMS and SP2 in every 200 m in 2016 and 2018 ORACLES campaigns, respectively. The lines are the mean value in every 200 m bin. Errorbars and grey shading represent the standard deviation in every 200 m bin.

Flights in 2016 ORACLES (Fig. 1, yellow lines) are in the region of 8-24° S and 0-15° E, traversing both the southern African Easterly Jet (AEJ-S) region and the continent anticyclone. As a result, aerosols around 600 -700 hPa in 2016 ORACLES include both less aged (<4 d) particles coming directly from the continent and highly aged (>10 d) particles transported from the west/north, resulting in a larger variation of plume age in each level as shown in Fig. 2a. At lower altitudes, aerosols are less aged than those in the 2018 campaign due to the subsidence near the Namibian coast (Fig. 1a). During the 2016 campaign, the cloud top is generally below 1.5 km. The 2018 ORACLES flights, represented by blue lines in Fig.

197　1, are primarily situated within the 0-15° S and 5-10° E coordinates. The cloud top in this

198　region is a bit lower than in 2016 campaign, centering around 1 km. This area generally

199　coincides with the region influenced by the southern African Easterly Jet (AEJ-S). BB aerosols

200　are lifted up to the free troposphere, transported westward by AEJ-S and then subside into the

201　marine boundary layer, rendering the distinct vertical age pattern that increases with the

202　decreasing altitude (Fig. 2c). Correspondingly, aerosols in the SEA region during BB season

203　exhibit distinct vertical distribution of chemical composition. From Fig. 2b and 2d, the vertical

204　profiles of chemical composition fractions are generally consistent during 2016 and 2018

205　ORACLES campaigns. In this section, we focused on the variation of OA and sulphate, two

206　components that dominate aerosol hygroscopicity in the SEA.

207　　　　OA constitutes the largest fraction of aerosol mass in ORACLES, approximately 60 %.

208　The OA mass fraction in both years shows little variation above 2 km; below this altitude, OA

209　mass fraction decreases with decreasing altitude, in contrast to the trend of the sulphate mass

210　fraction. The OA/BC ratio, representing the OA mass concentration normalised by that of BC

211　to remove the dilution effect during transport, differs in 2016 and 2018. While 2018 data shows

212　a clear decrease in OA/BC with decreasing altitude, the decrease was less pronounced in 2016,

213　showing considerable variation at identical altitudes. Dobracki et al. (2022) used RH as an

214　indicator to investigate the importance of thermodynamic partitioning in OA/BC changes

215　during the 2016 ORACLES campaign, concluding that it accounts for no more than 10 % of

216　the changes. The dominant factor is believed to be the oxidation of OA through fragmentation.

217　A similar result is found in this study using temperature as an indicator, as shown in Fig. 3a.

218　Please note Fig. 3 only considers OA above 1.4 km and temperature > 0 ℃ to minimize the

219　marine influence and to exclude possible ice nucleation. The OA/BC ratio in the 2016

220　ORACLES campaign did not show a clear decrease with increasing temperature, as NO_3/BC

221　did, which is a result of thermodynamic repartition to the gas phase. However, in the 2018

222   ORACLES campaign, we did notice a significant decrease of OA/BC with increasing

223   temperature (Fig. 3b). The OA/BC decreased ~70 % from 9.7±3.1 for temperature 0-4 °C to

224   2.9±0.9 for temperature > 20 °C, only slightly lower than the decrease of NO_3/BC, ~85 %. Yet,

225   we cannot simply attribute the OA/BC changes to thermodynamic repartition while

226   disregarding the effect of ageing or OA oxidation. In 2018, temperature and plume age are

227   closely correlated (Pearson correlation coefficient of 0.51), and the decrease in OA/BC is

228   accompanied by ageing (Pearson correlation coefficient of 0.57), as shown in Fig. 2a and b.

229   We utilized the oxidation state to differentiate between the effects of thermodynamic

230   repartition and OA oxidation. Figure 4 shows the Van Krevelen diagrams (H/C vs. O/C, Ng et

231   al., 2011) for aerosols under temperatures > 20 °C and 0-4 °C. The estimated carbon oxidation

232   state (OS_C), defined as $OS_C = 2O/C - H/C$, can also indicate different OA volatility regimes, with

233   OSc of -2.0− -1.5 for HOA (hydrocarbon-like OA), -1.75− -0.75 for BBOA (biomass burning

234   OA), -1.0−0.0 for SV-OOA (semi-volatile oxidized OA), and 0.0−1.0 for LV-OOA (low

235   volatility oxidized OA) (Donahue et al., 2012; Kroll et al., 2011). If thermodynamic repartition

236   plays a more crucial role, the OA remaining under higher temperature would be less volatile

237   due to evaporation of more volatile OA. Notably, we found the opposite. From Fig. 4, aerosols

238   under temperature > 20 °C (lower altitudes) are generally more volatile than those at

239   temperature 0-4 °C (higher altitudes). This indicates that thermodynamic repartition is not a

240   dominant factor in OA/BC changes, and that the OA oxidation through fragmentation is more

241   important in OA/BC changes in 2018, consistent with the 2016 campaign as well as results in

242   Dobracki et al. (2022). This is also in line with the findings of Dang et al. (2022) which found

243   less organics in aerosols collected on filters associated with more aged plumes and more

244   rounded and viscous organics on filters sampled from less aged plumes. For OA below 1.4 km,

245   aqueous phase reactions and cloud scavenging might also contribute to the loss of OA during

246   the entrainment and within the MBL (Che et al., 2021; Wu et al., 2020).

247
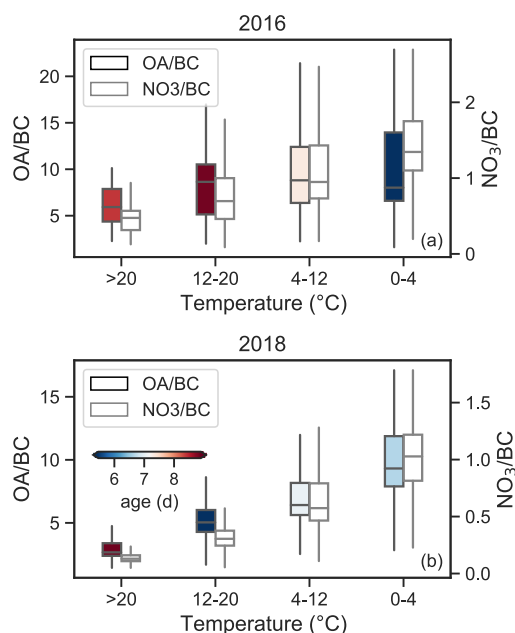
Figure 3. OA/BC (black outline) and NO3/BC (grey outline) mass ratios as a function of

ambient temperature in 2016 (a) and 2018 (b) ORACLES campaign, for altitude > 1.4 km and

temperature > 0 °C. The boxes represent the 10th percentile, 25th percentile, median, 75th

percentile, and 90th percentile.

252
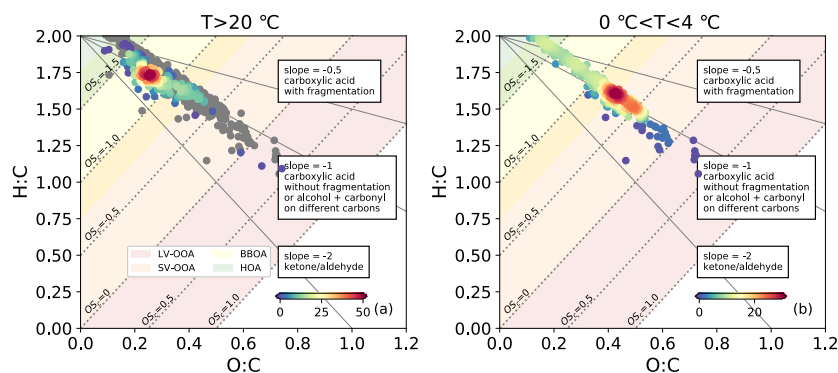
Figure 4. Van Krevelen diagram (H/C vs. O/C) for aerosols with temperature higher than 20 °C

(a) and with temperature lower than 4 °C (b). The color scale indicates the density of the data

255   in each plot. The grey dots in (a) are the Van Krevelen diagram of aerosols with temperature

256   lower than 4 °C, the same as (b).

257   The variation of sulphate mass fraction remains largely constant above 2 km, and below

258   2 km, increases with decreasing altitudes. The higher sulphate fraction at lower altitudes is

259   consistent with the observations from CLARIFY-2017 (CLoud-Aerosol-Radiation Interaction

260   and Forcing for Year 2017) campaign (Wu et al., 2020), which was conducted downwind of

261   ORACLES in the SEA ocean. This higher sulphate fraction at lower altitudes results from the

262   increase of SO_4/BC and decrease of OA/BC. SO_4/BC ratio generally remains constant above

263   800 m in both years' campaign. However, for 2016 ORACLES campaign, where there are

264   samples below 800 m, the ratio shows an increase with decreasing altitude. This increase could

265   indicate a sulphate contribution from the ocean, either in the form of sea-salt sulphate or

266   through dimethylsulfide (DMS) emitted by marine phytoplankton. The latter can contribute to

267   non-sea-salt sulphate by oxidizing to SO_2 and further to sulphate (Mayer et al., 2020; Alexander

268   et al., 2005). Notably, part of the 2016 flight region, especially the SEA offshore of Namibia,

269   is known as an upwelling region with high DMS emissions (Andreae et al., 1995). Klopper et

270   al. (2020) have attributed 57 % of sulphate to sea salt and 43 % to non-sea-salt sulphate along

271   the Namibian coast. These findings align with model simulations showing that DMS is the third

272   largest CCN source in the SEA up to 2 km (Che et al., 2022b).

273   Furthermore, BC mass constitutes approximately 10 % of the PM_1 mass fraction,

274   indicating the large influence of BB in this region. The nitrate mass fraction increases with

275   increasing altitude in all layers, which is consistent with the findings of CLARIFY, and can be

276   explained by the shift of gas-particle partitioning of the HNO_3-NH_3-NH_4NO_3 system towards

277   the aerosol phase at the lower temperatures found at higher altitudes (Wu et al., 2020). The

278   mass fraction of ammonium stays stable with height, approximately 5 %.

279   3.2 Aerosol hygroscopicity in SEA in 2016 and 2018 ORACLES
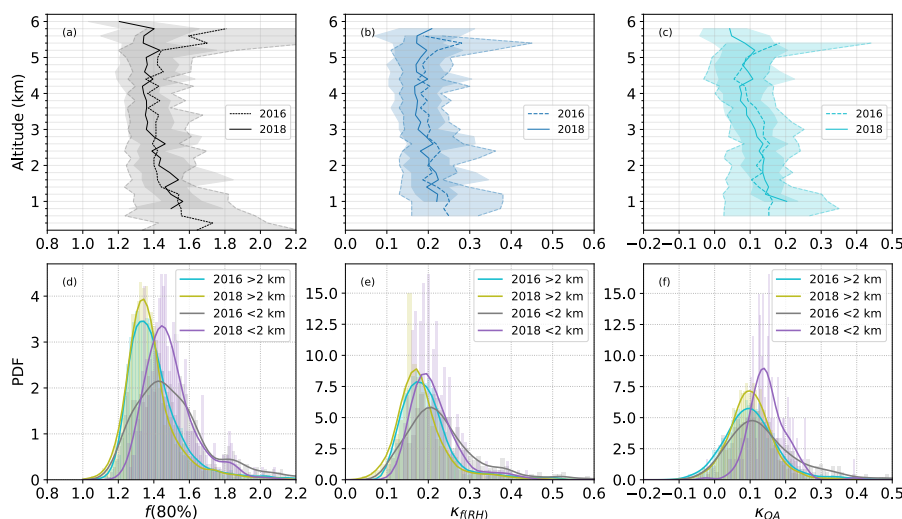
Figure 5. Vertical profiles and PDF of $f(80\%)$ (a, d), $\kappa_{f(RH)}$ (b, e), and κ_{OA} (c, f) for aerosols in the 2016 (dotted line) and 2018 (solid line) ORACLES campaign. Dashed lines in a, b, and c represent the 10th percentile, mean, and 90th percentile, respectively.

In general, the aerosol hygroscopicity stays stable above 2 km in both years' campaigns; while below 2 km, aerosols become more hygroscopic at lower altitudes (Fig. 5). This is consistent with the vertical variation of sulphate and OA mass fraction, i.e. more sulphate and less OA at lower altitudes. The probability density function (PDF) distributions of $f(80\%)$ and $\kappa_{f(RH)}$ are similar in the 2016 and 2018 campaigns, with larger variations and higher values of the aerosol hygroscopicity PDF under 2 km (Fig. 5d and 5e). For $f(80\%)$ below 2 km, a primary mode with a diameter around 1.45 is evident, but there is also a second mode with a diameter around 1.81 for aerosols in both years. While the second mode is subtle, it can be identified in the PDF of $\kappa_{f(RH)}$ (Fig. 5e). This suggests the presence of highly hygroscopic substances and could indicate marine influence, as most aerosols below 2 km are within the MBL. For aerosols above 2 km, the mean and standard deviation of $f(80\%)$ and $\kappa_{f(RH)}$ are 1.40±0.17 and 0.19±0.07 (Fig. 5 and Table S2), respectively, belonging to less hygroscopic particles (Liu et al., 2011).

296   These values are generally lower than those for marine aerosols (Zieger et al., 2010; Carrico et

297   al., 2003), higher than dust and polluted dust particles (Bukowiecki et al., 2016; Zhang et al.,

298   2015a), and consistent with the median level of the hygroscopicity for smoke-dominated

299   aerosols found in the literature. They are comparable to the $f(80\%)$ of 1.37 for smoke from

300   lightly-wooded savanna fires in Australia (D_P<3 μm) (Gras et al., 1999), and the $f(82\%)$ of 1.40

301   for BBAs from forest fires in northeast US (Wang et al., 2007); while slightly higher than the

302    $f(80\%)$ of BBAs in Brazil (SCAR-B, D_P<4 μm) (Kotchenruther and Hobbs, 1998). For aerosols

303   below 2 km, they belong to more hygroscopic particles (Liu et al., 2011). The mean and

304   standard deviation of $f(80\%)$ and $\kappa_{f(RH)}$ are 1.51±0.22 and 0.23±0.08, respectively, which

305   belong to the upper ranges of BBA hygroscopicity in the literature. These values are

306   comparable to the $f(80\%)$ of 1.42±0.05 for smoke collected between 10 and 50 min of emission

307   in Africa (SAFARI, D_P<5 μm) (Magi and Hobbs, 2003), the $f(80\%)$ of 1.43±0.12 in a

308   background station in the Yangtze River Delta of China (Zhang et al., 2015a), and the $\kappa_{f(RH)}$ of

309   0.22±0.04 in a rural site in southern China (Kuang et al., 2021); while lower than the $f(85\%)$

310   of 1.60±0.20 for BBAs in East Asia during ACE-Asia (Asian Pacific regional aerosol

311   characterization experiment) (Kim et al., 2006), the $f(85\%)$ of 1.58±0.21 for agricultural

312   burning in INDOEX (Indian Ocean Experiment) (Sheridan et al., 2002), the $f(80\%)$ of

313   1.66±0.08 for fresh smoke (within 10 min from emission) in Africa (Magi and Hobbs, 2003).

314   Comparing to the κ obtained from CCN measurements at a similar location in August 2017

315   ORACLES (Kacarab et al., 2020), our results are ~ 30 % lower. This difference is expected

316   because κ values obtained under supersaturated conditions are typically larger than those from

317   sub-saturated conditions (Petters and Kreidenweis, 2007). This highlights the significance of

318   using the appropriate κ for sub-saturated and supersaturated investigations, such as when

319   examining aerosol liquid water content and cloud condensation nuclei activation (Rastak et al.,

320   2017; Petters and Kreidenweis, 2007).

321   The mean κ_{OA} (±1 standard deviation) is 0.11±0.08, with the 25th and 75th percentiles

322   of 0.06 and 0.16. From the vertical profiles, more hygroscopic OA are generally more aged,

323   highly oxidized, and usually located at lower altitudes (Fig. 2 and 5). In addition, we observed

324   a slight increase in κ_{OA} with volatility in 2016, with a Pearson correlation coefficient of -0.35

325   between κ_{OA} and OSc, contrasting the conventional understanding that the most volatile

326   compounds have the least hygroscopicity. This trend has been observed, albeit rarely, in field

327   and laboratory studies (e.g. Cerully et al., 2015; AsaAwuku et al., 2009). It may be related to

328   fragmentation during OA oxidation, where the highly aged and low volatile OA may dissociate

329   into more volatile fragments that are still highly functionalized and hygroscopic. However, in

330   general, no clear correlation has been found between κ_{OA} with altitude or oxidation level.

331   We noted a portion of highly aged aerosols (> 10 d) in 2016 having high OA/BC (> 12,

332   corresponding OA mass fraction > 50 %), in contrast to the general trend that more aged

333   aerosols correspond to smaller OA/BC (Fig. 2). About 95 % of these aerosols are above 3 km

334   and have a slightly lower f_{44} than the campaign average (Fig. S1a). Approximately 60 % belong

335   to LV-OOA with OSc > 0 and 40 % are SV-OOA (Fig. S1b). As shown in Fig. S1c, the κ_{OA}

336   values are smaller for these aerosols compared to the whole 2016 campaign, which is consistent

337   with previous studies that κ_{OA} is lower for less oxidized OA (Kuang et al., 2020; Rastak et al.,

338   2017; Mei et al., 2013); though we do not observe such correlation for the entire campaign. We

339   hypothesize that thermodynamical repartitioning has played a role, i.e. less-oxidized materials

340   condensed onto pre-existing OA under low temperature at high altitudes, resulting in smaller

341   f_{44} values and contributing to SV-OOA. These less-oxidized materials are generally less

342   functionalized and less hygroscopic, which would lead to a lower κ_{OA}.

343   3.3 Relationship with chemical composition and κ_{OA}

344   3.3.1 Comparison with various campaigns

345
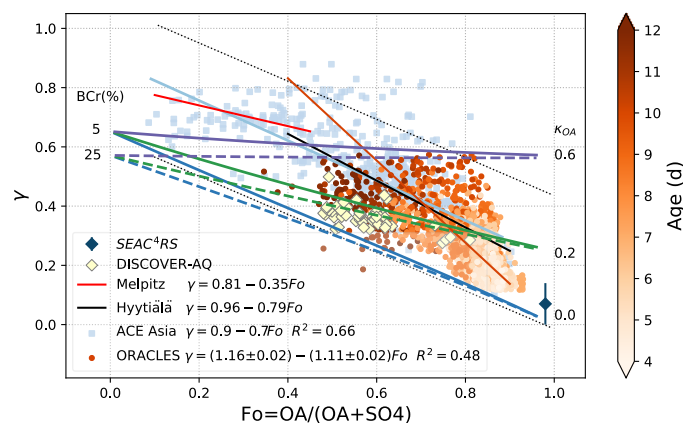
Figure 6. γ versus Fo in various campaigns and for internally mixed OA-$(NH_4)_2SO_4$-BC

mixtures. Fo represents the ratio of mass concentrations of OA to OA and SO_4^{2-}. Solid lines in

light blue and brown represent the linear fits for ACE-Asia and ORACLES, respectively.

Dotted grey lines show the 95% prediction bands for the ACE-Asia data, in light blue

rectangles, taken from Quinn et al. (2005). Colorbar represents the plume age (days) in

ORACLES. Data for SEAC[4]RS is shown by blue diamond, taken from Shingler et al. (2016).

DISCOVER-AQ data is shown by yellow diamonds, taken from NASA Langley Research

Center Atmospheric Science Data Center (Atmospheric Science Data Center, 2015). Fitting

lines for two European sites Melpitz (solid red line) and Hyytiälä (solid black line) are from

Zieger et al. (2015). Blue, green, and purple lines represent results for internally mixed OA-

$(NH_4)_2SO_4$-BC mixtures with 1) a range of BC mass fraction (BCr, solid for 5% and dashed

for 25%) and 2) OA with κ_{OA} of 0 (blue), 0.2 (green), and 0.6 (purple) from Mie calculations

assuming a lognormal size distribution with a geometric mean diameter D_{gn} of 150 nm and a

standard deviation σ_{sg} of 1.5.

Quinn et al. (2005) proposed a parameterization quantifying the relationship between γ

and Fo, the ratio of mass concentrations of OA to OA and SO_4^{2-}, based on measurements in

ACE-Asia. We applied the parameterization to ORACLES measurements and as shown in Fig.

18

363   6, our data are well within the 95% prediction confidence intervals. We further investigated the

364   γ-Fo dependence of BBAs from DISCOVER-AQ and SEAC[4]RS (Shingler et al., 2016) and

365   continental aerosols from the central European station Melpitz and a boreal site Hyytiälä in

366   Finland (Zieger et al., 2014, 2015), all showed good overlap with those from ACE-Asia and

367   ORACLES. The linear regression for ORACLES, $\gamma = (1.16\pm0.02) - (1.11\pm0.02)\cdot Fo$, retrieved

368   from an orthogonal fit by taking the standard deviation as the input for uncertainty calculation,

369   is very similar to those in Hyytiälä and ACE-Asia, though the slope is slightly lower.

370   We explored the γ-Fo relationship with the Mie model and found that the relationship

371   observed can be largely explained by aerosol chemical composition and OA hygroscopicity.

372   The γ values were calculated with the scattering coefficients simulated at both dry conditions

373   and 80 % RH were performed with Mie model for internally mixed OA-$(NH_4)_2SO_4$-BC

374   mixtures with assumed BC mass ratio (BCr, 5 % and 25 %), and κ_{OA} values (0-0.6), which

375   encompass the ranges observed in ORACLES (refer to Sect. 3.2 for κ_{OA} values). The PNSD

376   was calculated following the lognormally distribution, with the geometric mean diameter (D_{gn})

377   and standard deviation (σ_{sg}) set to D_{gn}=150 nm and $\sigma_{sg} = 1.6$, respectively. As shown in Fig. 6

378   (solid and dashed purple, green, and blue lines), simulated curves can capture most of the

379   observations. Fo and κ_{OA} dominant γ, and BC shows a small negative impact. It is noteworthy

380   that the (negative) slope of the γ-Fo relationship increases with increasing κ_{OA} up to κ_{OA} values

381   of 0.6, where γ exhibits little variation with Fo. Therefore, we conclude that the variation of

382   BBA hygroscopicity with ageing in the SEA is mainly due to changes in chemical composition,

383   particularly sulphate and OA, as well as the variation of OA hygroscopicity during transport.

384   The higher BC fraction in aged aerosols compared to less aged ones has slightly decreased the

385   hygroscopicity of aged aerosols.

386   3.3.2 Parameterization of γ using Mie simulations of internally mixed OA-$(NH_4)_2SO_4$-

387   BC mixtures

388
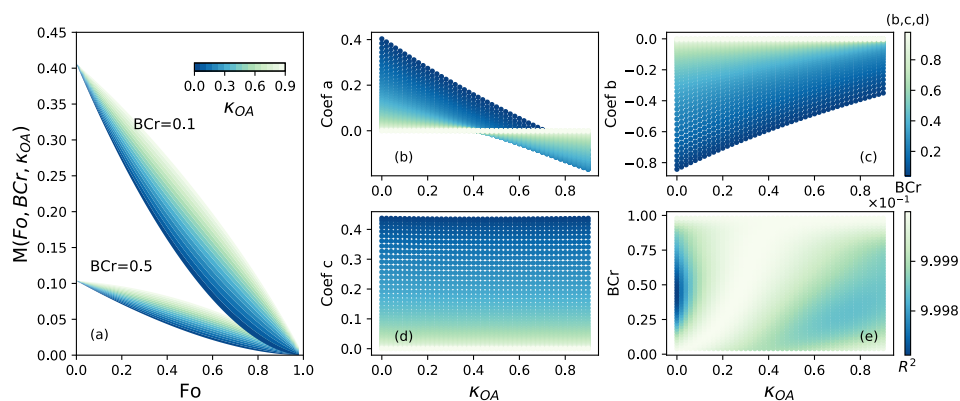
Figure 7. (a) Variations of M(Fo,κ_{OA},BCr) with Fo coloured by κ_{OA} at BCr of 0.1 and 0.5,

respectively, for internally mixed OA-$(NH_4)_2SO_4$-BC mixtures. M(Fo,κ_{OA},BCr) is the product

of γ(Fo,κ_{OA}=0,BCr) and γ(Fo,κ_{OA},BCr) for each κ_{OA} value. Fo represents the ratio of the mass

concentration of OA to that of OA and SO_4^{2-}. BCr is the mass ratio of BC. (b,c,d) Variation of

coefficients a, b, and c with κ_{OA} and BCr. The coefficients a, b, and c are the fitted parameters

of the quadratic regression between M(Fo,κ_{OA},BCr) and Fo for each κ_{OA} and BCr. (e) The R^2

(colorbar) of the M(Fo,κ_{OA},BCr) regression with Fo as a function of κ_{OA} and BCr.

Mie simulations are performed for internally mixed OA-$(NH_4)_2SO_4$-BC mixtures to

obtain the scattering coefficient of dry and humidified aerosols. We assume PNSD to be a log-

normal distribution with D_{gn}=150 nm and σ_{sg} = 1.6, as the approximation of the D_{gn} and σ_{sg} in

ORACLES 2016 and 2018 campaigns. The RH and RH_{ref} is set as 80 % and 0, respectively.

The γ is then calculated following Eq. 2. The Fo, κ_{OA}, and BCr are varied from 0 to 1, 0 to 0.9,

and 0 to 1, respectively, all with a span of 0.02. Taking γ(Fo,κ_{OA}=0,BCr) as the baseline (refer

to solid and dashed blue lines in Fig. 6), we calculated the product M(Fo,κ_{OA},BCr) of

γ(Fo,κ_{OA}=0,BCr) and γ(Fo,κ_{OA},BCr) for each κ_{OA} and BCr, i.e. M(Fo,κ_{OA},BCr)=

γ(Fo,κ_{OA}=0,BCr)* γ(Fo,κ_{OA},BCr), and found that the relationship between M(Fo,κ_{OA},BCr) and

Fo can be well fitted into a quadratic (second-order) polynomial function, i.e. M(Fo,κ_{OA},BCr)

= aFo^2+bFo+c (Fig. 7a). The variation of M(Fo,κ_{OA},BCr) with Fo and the R^2 of the regression

407   are shown in Fig. 7a and 7e, respectively. The fitted coefficients a, b, and c, as shown in Fig.

408   7b, 7c, and 7d, coincidentally fit well as quadratic functions of κ_{OA}, whose coefficients, in turn,

409   can be well fitted into a fifth-order polynomial function of BCr. Results are shown in Fig. S3

410   in the supplement. In sum, the M(Fo,κ_{OA},BCr) can be parameterized as:

$$M(F_o, \kappa_{OA}, BCr) = \sum_{\substack{i \leq 2 \\ j \leq 2 \\ k \leq 5}} a_{ijk} BCr^k \kappa_{OA}^j F_o^i \tag{4}$$

411   Similarly, γ(Fo,κ_{OA}=0,BCr) can be well fitted into a quadratic function of Fo with coefficients

412   that fit well with a fifth-order polynomial function of BCr:

$$\gamma(F_o, \kappa_{OA} = 0, BCr) = \sum_{\substack{i \leq 2 \\ k \leq 5}} a_{ik} BCr^k F_o^i \tag{5}$$

413   Equations 4 and 5 in matrix format are referred to Eq. S1 and S2 in the supplement,

414   respectively. Values of coefficients a_{ijk} and a_{ik} are shown in Table S3. Therefore,

415   γ(Fo,κ_{OA},BCr) can be calculated as the ratio of M(Fo,κ_{OA},BCr) to γ(Fo,κ_{OA}=0,BCr):

$$\gamma(Fo, \kappa_{OA}, BCr) = M(F_o, \kappa_{OA}, BCr) / \gamma(F_o, \kappa_{OA} = 0, BCr) \tag{6}$$

416   The f(RH) can then be calculated with Eq. 2. We evaluated this parameterization by comparing

417   the predicted and measured f(80%) in ORACLES 2016 and 2018 campaigns. The predicted

418   f(80%) is calculated with Eq. 6 with Fo, κ_{OA}, and BCr as inputs and Eq. 2 with the dry and

419   humidified RHs measured in both campaigns. Note the mean BC mass ratio for each year has

420   been used in the calculation, as little difference has been observed using the temporal BCr and

421   mean BCr. Good correlation of measured and predicted f(80%) has been achieved for both

422   years' campaign, as shown in Fig. 8a. This indicates that the internally mixed OA-$(NH_4)_2SO_4$-

423   BC mixture with PNSD (D_{gn}=150 nm and σ_{sg} = 1.6) is a good approximation of aerosols with

424   respect to the f(RH) prediction in 2016 and 2018 ORACLES campaign. The influence of PNSD

425   on f(RH) is small and discussed in Section S1 in the supplement.

426
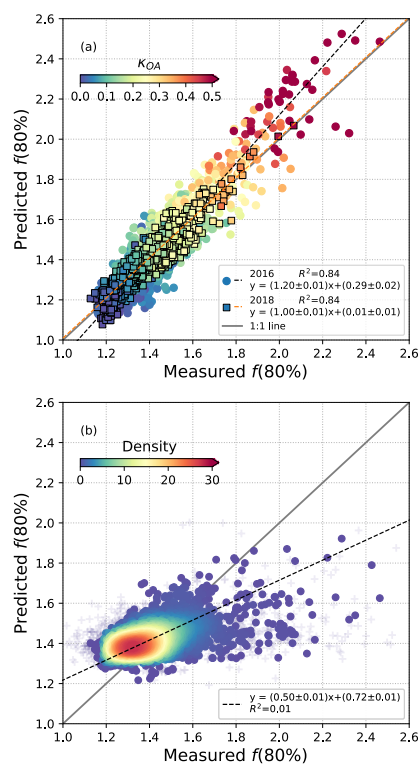
Figure 8. Measured $f(80\%)$ vs predicted $f(80\%)$ using the γ parameterization for internally mixed OA-$(NH_4)_2SO_4$-BC mixtures. The $f(80\%)$ in subplot (a) is calculated with κ_{OA} values coloured by κ_{OA}, and in subplot (b) is predicted with the mean κ_{OA} values. Black and orange dashed lines in subplot (a) represent the ordinary linear regression for 2016 and 2018, respectively. The black dashed line in subplot (b) represents the ordinary linear regression for the two years. Grey solid line is the 1:1 line.

3.3.3 Sensitivity of aerosol scattering enhancement to κ_{OA}

Due to the chemical complexity of OA, the κ_{OA} values of particles are not easily obtained. Various hygroscopicity parameterizations have been proposed in previous studies, most of which are parameterized with chemical composition, e.g. organics or inorganics fraction, and a constant assumed κ_{OA} value. Few studies consider the variation of κ_{OA} (Zhang

438   et al., 2015b; Huang et al., 2022). While these parameterizations can represent their

439   observations well, they may not be suitable for situations with different κ_{OA} values. Therefore,

440   in this section, the influence of κ_{OA} on the prediction of f(RH) is analyzed. We calculated the

441   f(80%) with the mean κ_{OA} in each campaign and the results are shown in Fig. 8b. The use of a

442   constant κ_{OA} average leads to a much smaller variation of the predicted f(80%) values, with

443   most of which concentrated around 1.3-1.4. Predicted f(80%) tend to overestimate lower

444   f(80%) values while underestimate higher f(80%) values. A slope of 0.50 and a R^2 of 0.01

445   indicates poor prediction in capturing the trend of f(80%). This indicates that using Fo, BCr,

446   and a constant κ_{OA} is insufficient for the prediction of f(RH), and that the variation of κ_{OA} need

447   to be considered, at least for situations where κ_{OA} has a large variation, such as in ORACLES.

448   To quantitively investigate the sensitivity of f(RH) to κ_{OA}, we calculated the deviation

449   of f(80%) with κ_{OA} for the OA-$(NH_4)_2SO_4$-BC mixture. As shown in Fig. 9, we observed that

450   κ_{OA} is positively correlated with f(80%). Additionally, the deviation of f(80%) is dependent on

451   the OA fraction (Fo), i.e. a higher OA fraction leads to a larger impact of κ_{OA} and consequently

452   a larger deviation of f(80%).

453   The 25th and 75th percentiles of Fo in 2016 and 2018 ORACLES campaign were 0.74

454   and 0.86, respectively. These are relatively high values and therefore result in relatively high

455   spread of f(80%). As well, the age of ORACLES OA spans from <4 days to > 10 days, during

456   which OA oxidation and fragmentation (as discussed in Section 3.2) takes place. These

457   processes alter the hygroscopicity of OA, causing the OA in ORACLES to contribute to large

458   variations of κ_{OA}. These large variations of κ_{OA}, combined with the relatively high OA fraction

459   (Fo), makes f(RH) highly sensitive to the κ_{OA} value. For aerosols with a κ_{OA} of 0.4 and a Fo of

460   0.86, the f(80%) can be 80 % higher compared to aerosols with hydrophobic OA, as shown in

461   Fig. 9. In other words, the aerosol scattering coefficients at 80 % RH are 80 % higher solely

462   because of the increase of OA hygroscopicity. This high sensitivity also explains the poor

463   prediction of $f(80\%)$ when using campaign mean κ_{OA} values, as shown in Fig. 8b. We further

464   analyzed the influence of κ_{OA} value on $f(80\%)$ for a relatively polluted site on the North China

465   Plain based on their κ_{OA} values (Kuang et al., 2020). Its κ_{OA} rises from 0.02 in the morning to

466   0.16 in the noon, combining its Fo of 0.86, the $f(80\%)$ can increase by 25 % when the κ_{OA} is

467   0.16 compared to it being 0.02. It means that the scattering coefficients at 80 % RH can be

468   25 % higher at noon compared to the morning solely due to the increase of OA hygroscopicity.

469   Many studies overlook the variability of κ_{OA} and instead use a constant κ_{OA} when analyzing

470   aerosol hygroscopicity or radiative forcing. As illustrated in Fig. 9, this can be reasonable when

471   the OA fraction is low and κ_{OA} exhibits minimal variation; however, in cases where these two

472   conditions are not met, κ_{OA} can significantly influence the scattering coefficients and hence

473   direct radiative forcing.
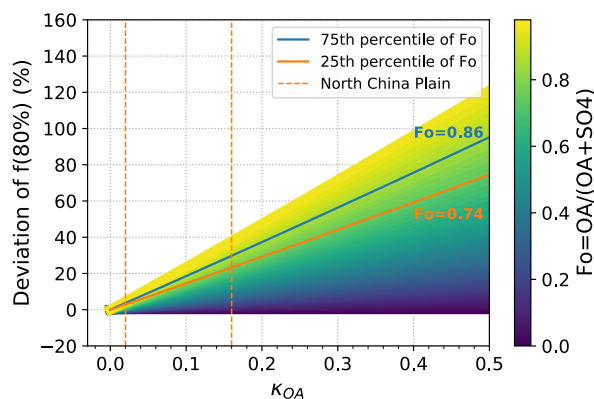
474

475   Figure 9. Sensitivity of $f(80\%)$ to κ_{OA}. The OA to OA + SO_4 ratio (Fo) is represented by the

476   colorbar. The blue and orange lines represent the variation at 75th and 25th percentile of Fo in

477   both years' ORACLES campaign, respectively. The pair of dashed orange lines represent the

478   range of κ_{OA} observed at the site on the North China Plain (Kuang et al., 2020).

479   **4 Conclusion**

480   The hygroscopicity of aerosols from the perspective of scattering enhancement over the

481   SEA Ocean during the BB season are investigated using measurements from the 2016 and 2018

482   ORACLES campaigns. The vertical distribution of aerosol hygroscopicity shows a consistent

483   pattern in both campaigns, remaining stable above 2 km; below 2 km, aerosols are more

484   hygroscopic at lower altitudes. Aerosols above 2 km have a mean and standard deviation of

485   $f(80\%)$ and $\kappa_{f(RH)}$ of 1.40±0.17 and 0.19±0.07, respectively, and are less hygroscopic.

486   Conversely, aerosols below 2 km are more hygroscopic, and have a mean and standard

487   deviation of $f(80\%)$ and $\kappa_{f(RH)}$ of 1.51±0.22 and 0.23±0.08, respectively, which are values at

488   the upper level of BBA hygroscopicity found in the literature. This variation of aerosol

489   hygroscopicity is consistent with the vertical variation of chemical composition. The OA and

490   sulphate mass fraction in both years show little variation above 2 km; while below this altitude,

491   OA decreases with decreasing altitude, while the sulphate mass fraction tends to increase. OA

492   oxidation through molecular fragmentation is the main mechanism for OA losses in the FT.

493   While the increase of sulphate in the MBL could indicate marine influence.

494   We retrieved κ_{OA} using Mie simulations. It shows a large variation, with the mean and

495   standard deviation being 0.11±0.08 and the 25th and 75th percentiles of 0.06 and 0.16,

496   respectively. No clear relationship was found between κ_{OA} and OA oxidation level; while a

497   slight increase in κ_{OA} with volatility is shown in 2016, which may be related to the

498   fragmentation during OA oxidation, where the highly aged and low volatile OA may dissociate

499   into more volatile fragments that are still highly functionalized and hygroscopic. In all, OA

500   hygroscopicity under sub-saturated conditions can be largely influenced by solubility,

501   molecular weight, molecular functional groups, and carbon number (Cai et al., 2021; Kuang et

502   al., 2020; Rastak et al., 2017; Rickards et al., 2013; Suda et al., 2012); to better understand the

503   variation of κ_{OA}, more molecular investigations are needed.

504   In comparison with other campaigns, we find the variation of aerosol hygroscopicity in

505   the SEA is mainly due to changes in chemical composition, particularly sulphate and OA, as

506   well as variations in OA hygroscopicity during transport. To quantitatively investigate this

507   relationship, we came up with a parameterization using Fo, BCr, and κ_{OA}, and the f(80%) from

508   Mie simulations for internally mixed OA-$(NH_4)_2SO_4$-BC mixture with PNSD (D_{gn}=150 nm

509   and σ_{sg}=1.6). This suggests that the internal mixture of OA-$(NH_4)_2SO_4$-BC is a good

510   approximation of aerosols with respect to the f(RH) prediction in 2016 and 2018 ORACLES

511   campaign.

512   Sensitivity study indicates that solely due to the increase in OA hygroscopicity

513   observed in our study, the aerosol scattering coefficients at 80 % RH can be amplified by 80 %.

514   Relying on the campaign's mean κ_{OA} value leads to a poor prediction of f(80%). The

515   dependence of f(RH) on κ_{OA} suggests that using a constant κ_{OA} can be acceptable when the OA

516   fraction is low and κ_{OA} demonstrates limited variations. However, in situations where these

517   two conditions are not met, κ_{OA} can significantly influence the scattering coefficients and thus

518   aerosol radiative effect. Therefore, accommodating the variability of κ_{OA} is advisable.

519

520   *Competing interests.* At least one of the (co-)authors is a guest member of the editorial board

521   of Atmospheric Chemistry and Physics for the special issue "New observations and related

522   modelling studies of the aerosol-cloud-climate system in the Southeast Atlantic and southern

523   Africa regions". The authors have no other competing interests to declare.

524

525   *Special issue statement.* This article is part of the special issue "New observations and related

526   modeling studies of the aerosol-cloud-climate system in the Southeast Atlantic and southern

527   Africa regions (ACP/AMT inter-journal SI)". It is not associated with a conference.

528

529   *Data Availability.* Data sets are publicly available via the digital object identifier provided

530   under   ORACLES   Science   Team   reference:

531   https://doi.org/10.5067/Suborbital/ORACLES/P3/2018_V2.

532

553

554

555 **References**

556 Alexander, B., Park, R. J., Jacob, D. J., Li, Q. B., Yantosca, R. M., Savarino, J., Lee, C. C.
557 W., and Thiemens, M. H.: Sulfate formation in sea-salt aerosols: Constraints from oxygen
558 isotopes, J. Geophys. Res. Atmospheres, 110, https://doi.org/10.1029/2004JD005659, 2005.

559 Andreae, M. O., Elbert, W., and de Mora, S. J.: Biogenic sulfur emissions and aerosols over
560 the tropical South Atlantic: 3. Atmospheric dimethylsulfide, aerosols and cloud condensation
561 nuclei, J. Geophys. Res. Atmospheres, 100, 11335–11356,
562 https://doi.org/10.1029/94JD02828, 1995.

563 Bukowiecki, N., Weingartner, E., Gysel, M., Coen, M. C., Zieger, P., Herrmann, E.,
564 Steinbacher, M., Ga̋ggeler, H. W., and Baltensperger, U.: A Review of More than 20 Years
565 of Aerosol Observation at the High Altitude Research Station Jungfraujoch, Switzerland
566 (3580 m asl), Aerosol Air Qual. Res., 16, 764–788,
567 https://doi.org/10.4209/aaqr.2015.05.0305, 2016.

568 Burgos, M. A., Andrews, E., Titos, G., Benedetti, A., Bian, H., Buchard, V., Curci, G.,
569 Kipling, Z., Kirkevåg, A., Kokkola, H., Laakso, A., Letertre-Danczak, J., Lund, M. T.,
570 Matsui, H., Myhre, G., Randles, C., Schulz, M., van Noije, T., Zhang, K., Alados-Arboledas,
571 L., Baltensperger, U., Jefferson, A., Sherman, J., Sun, J., Weingartner, E., and Zieger, P.: A
572 global model–measurement evaluation of particle light scattering coefficients at elevated
573 relative humidity, Atmospheric Chem. Phys., 20, 10231–10258, https://doi.org/10.5194/acp-
574 20-10231-2020, 2020.

575 Cai, M., Liang, B., Sun, Q., Liu, L., Yuan, B., Shao, M., Huang, S., Peng, Y., Wang, Z., Tan,
576 H., Li, F., Xu, H., Chen, D., and Zhao, J.: The important roles of surface tension and growth
577 rate in the contribution of new particle formation (NPF) to cloud condensation nuclei (CCN)
578 number concentration: evidence from field measurements in southern China, Atmospheric
579 Chem. Phys., 21, 8575–8592, https://doi.org/10.5194/acp-21-8575-2021, 2021.

580 Carrico, C. M., Kus, P., Rood, M. J., Quinn, P. K., and Bates, T. S.: Mixtures of pollution,
581 dust, sea salt, and volcanic aerosol during ACE-Asia: Radiative properties as a function of
582 relative humidity, J. Geophys. Res. Atmospheres, 108,
583 https://doi.org/10.1029/2003JD003405, 2003.

584 Cerully, K. M., Bougiatioti, A., Hite, J. R. J., Guo, H., Xu, L., Ng, N. L., Weber, R., and
585 Nenes, A.: On the link between hygroscopicity, volatility, and oxidation state of ambient and
586 water-soluble aerosols in the southeastern United States, Atmospheric Chem. Phys., 15,
587 8679–8694, https://doi.org/10.5194/acp-15-8679-2015, 2015.

588 Che, H., Zhang, X., Zhang, L., Wang, Y., Zhang, Y., Shen, X., Ma, Q., Sun, J., and Zhong, J.:
589 Prediction of size-resolved number concentration of cloud condensation nuclei and long-term
590 measurements of their activation characteristics, Sci. Rep., 7, 5819,
591 https://doi.org/10.1038/s41598-017-05998-3, 2017.

592   Che, H., Segal-Rozenhaimer, M., Zhang, L., and Dang, C.: Transport and aging of biomass
593   burning aerosols in the South-eastern Atlantic Ocean, Commun. Earth Environ., Accepted,
594   2021.

595   Che, H., Segal-Rozenhaimer, M., Zhang, L., Dang, C., Zuidema, P., Dobracki, A., Sedlacek,
596   A. J., Coe, H., Wu, H., Taylor, J., Zhang, X., Redemann, J., and Haywood, J.: Cloud
597   processing and weeklong ageing affect biomass burning aerosol properties over the south-
598   eastern Atlantic, Commun. Earth Environ., 3, 182, https://doi.org/10.1038/s43247-022-
599   00517-3, 2022a.

600   Che, H., Stier, P., Watson-Parris, D., Gordon, H., and Deaconu, L.: Source attribution of
601   cloud condensation nuclei and their impact on stratocumulus clouds and radiation in the
602   south-eastern Atlantic, Atmospheric Chem. Phys. Discuss., 1–26, https://doi.org/10.5194/acp-
603   2022-43, 2022b.

604   Chen, J., Zhao, C. S., Ma, N., and Yan, P.: Aerosol hygroscopicity parameter derived from
605   the light scattering enhancement factor measurements in the North China Plain, Atmospheric
606   Chem. Phys., 14, 8105–8118, https://doi.org/10.5194/acp-14-8105-2014, 2014.

607   Cotterell, M. I., Willoughby, R. E., Bzdek, B. R., Orr-Ewing, A. J., and Reid, J. P.: A
608   complete parameterisation of the relative humidity and wavelength dependence of the
609   refractive index of hygroscopic inorganic aerosol particles, Atmospheric Chem. Phys., 17,
610   9837–9851, https://doi.org/10.5194/acp-17-9837-2017, 2017.

611   Covert, D. S., Charlson, R. J., and Ahlquist, N. C.: A Study of the Relationship of Chemical
612   Composition and Humidity to Light Scattering by Aerosols, J. Appl. Meteorol., 11, 968–976,
613   https://doi.org/10.1175/1520-0450(1972)011<0968:ASOTRO>2.0.CO;2, 1972.

614   Cubison, M. J., Ortega, A. M., Hayes, P. L., Farmer, D. K., Day, D., Lechner, M. J., Brune,
615   W. H., Apel, E., Diskin, G. S., Fisher, J. A., Fuelberg, H. E., Hecobian, A., Knapp, D. J.,
616   Mikoviny, T., Riemer, D., Sachse, G. W., Sessions, W., Weber, R. J., Weinheimer, A. J.,
617   Wisthaler, A., and Jimenez, J. L.: Effects of aging on organic aerosol from open biomass
618   burning smoke in aircraft and laboratory studies, Atmospheric Chem. Phys., 11, 12049–
619   12064, https://doi.org/10.5194/acp-11-12049-2011, 2011.

620   Day, D. E., Hand, J. L., Carrico, C. M., Engling, G., and Malm, W. C.: Humidification
621   factors from laboratory studies of fresh smoke from biomass fuels, J. Geophys. Res.
622   Atmospheres, 111, https://doi.org/10.1029/2006JD007221, 2006.

623   DeCarlo, P. F., Slowik, J. G., Worsnop, D. R., Davidovits, P., and Jimenez, J. L.: Particle
624   Morphology and Density Characterization by Combined Mobility and Aerodynamic
625   Diameter Measurements. Part 1: Theory, Aerosol Sci. Technol., 38, 1185–1205,
626   https://doi.org/10.1080/027868290903907, 2004.

627   Ervens, B., Cubison, M., Andrews, E., Feingold, G., Ogren, J. A., Jimenez, J. L., DeCarlo, P.,
628   and Nenes, A.: Prediction of cloud condensation nucleus number concentration using
629   measurements of aerosol size distributions and composition and light scattering enhancement
630   due to humidity, J. Geophys. Res. Atmospheres, 112, https://doi.org/10.1029/2006JD007426,
631   2007.

632   Gras, J. L., Jensen, J. B., Okada, K., Ikegami, M., Zaizen, Y., and Makino, Y.: Some optical
633   properties of smoke aerosol in Indonesia and tropical Australia, Geophys. Res. Lett., 26,
634   1393–1396, https://doi.org/10.1029/1999GL900275, 1999.

635   Gysel, M., Crosier, J., Topping, D. O., Whitehead, J. D., Bower, K. N., Cubison, M. J.,
636   Williams, P. I., Flynn, M. J., McFiggans, G. B., and Coe, H.: Closure study between chemical
637   composition and hygroscopic growth of aerosol particles during TORCH2, Atmospheric
638   Chem. Phys., 7, 6131–6144, https://doi.org/10.5194/acp-7-6131-2007, 2007.

639   Haywood, J., Bush, M., Abel, S., Claxton, B., Coe, H., Crosier, J., Harrison, M., Macpherson,
640   B., Naylor, M., and Osborne, S.: Prediction of visibility and aerosol within the operational
641   Met Office Unified Model. II: Validation of model performance using observational data, Q.
642   J. R. Meteorol. Soc., 134, 1817–1832, https://doi.org/10.1002/qj.275, 2008.

643   Howell, S. G., Freitag, S., Dobracki, A., Smirnow, N., and Sedlacek III, A. J.: Undersizing of
644   aged African biomass burning aerosol by an ultra-high-sensitivity aerosol spectrometer,
645   Atmospheric Meas. Tech., 14, 7381–7404, https://doi.org/10.5194/amt-14-7381-2021, 2021.

646   Huang, S., Wu, Z., Wang, Y., Poulain, L., Höpner, F., Merkel, M., Herrmann, H., and
647   Wiedensohler, A.: Aerosol Hygroscopicity and its Link to Chemical Composition in a
648   Remote Marine Environment Based on Three Transatlantic Measurements, Environ. Sci.
649   Technol., https://doi.org/10.1021/acs.est.2c00785, 2022.

650   Kacarab, M., Thornhill, K. L., Dobracki, A., Howell, S. G., O'Brien, J. R., Freitag, S.,
651   Poellot, M. R., Wood, R., Zuidema, P., Redemann, J., and Nenes, A.: Biomass burning
652   aerosol as a modulator of the droplet number in the southeast Atlantic region, Atmospheric
653   Chem. Phys., 20, 3029–3040, https://doi.org/10.5194/acp-20-3029-2020, 2020.

654   Kim, J., Yoon, S.-C., Jefferson, A., and Kim, S.-W.: Aerosol hygroscopic properties during
655   Asian dust, pollution, and biomass burning episodes at Gosan, Korea in April 2001, Atmos.
656   Environ., 40, 1550–1560, https://doi.org/10.1016/j.atmosenv.2005.10.044, 2006.

657   Klopper, D., Formenti, P., Namwoonde, A., Cazaunau, M., Chevaillier, S., Feron, A.,
658   Gaimoz, C., Hease, P., Lahmidi, F., Mirande-Bret, C., Triquet, S., Zeng, Z., and Piketh, S. J.:
659   Chemical composition and source apportionment of atmospheric aerosols on the Namibian
660   coast, Atmospheric Chem. Phys., 20, 15811–15833, https://doi.org/10.5194/acp-20-15811-
661   2020, 2020.

662   Kotchenruther, R. A. and Hobbs, P. V.: Humidification factors of aerosols from biomass
663   burning in Brazil, J. Geophys. Res. Atmospheres, 103, 32081–32089,
664   https://doi.org/10.1029/98JD00340, 1998.

665   Kuang, Y., Xu, W., Tao, J., Ma, N., Zhao, C., and Shao, M.: A Review on Laboratory Studies
666   and Field Measurements of Atmospheric Organic Aerosol Hygroscopicity and Its
667   Parameterization Based on Oxidation Levels, Curr. Pollut. Rep., 6, 410–424,
668   https://doi.org/10.1007/s40726-020-00164-2, 2020.

669   Kuang, Y., Huang, S., Xue, B., Luo, B., Song, Q., Chen, W., Hu, W., Li, W., Zhao, P., Cai,
670   M., Peng, Y., Qi, J., Li, T., Wang, S., Chen, D., Yue, D., Yuan, B., and Shao, M.: Contrasting
671   effects of secondary organic aerosol formations on organic aerosol hygroscopicity,

672   Atmospheric Chem. Phys., 21, 10375–10391, https://doi.org/10.5194/acp-21-10375-2021,
673   2021.

674   Lambe, A. T., Onasch, T. B., Massoli, P., Croasdale, D. R., Wright, J. P., Ahern, A. T.,
675   Williams, L. R., Worsnop, D. R., Brune, W. H., and Davidovits, P.: Laboratory studies of the
676   chemical composition and cloud condensation nuclei (CCN) activity of secondary organic
677   aerosol (SOA) and oxidized primary organic aerosol (OPOA), Atmospheric Chem. Phys., 11,
678   8913–8928, https://doi.org/10.5194/acp-11-8913-2011, 2011.

679   Liu, P., Song, M., Zhao, T., Gunthe, S. S., Ham, S., He, Y., Qin, Y. M., Gong, Z., Amorim, J.
680   C., Bertram, A. K., and Martin, S. T.: Resolving the mechanisms of hygroscopic growth and
681   cloud condensation nuclei activity for organic particulate matter, Nat. Commun., 9, 1–10,
682   https://doi.org/10.1038/s41467-018-06622-2, 2018.

683   Liu, P. F., Zhao, C. S., Göbel, T., Hallbauer, E., Nowak, A., Ran, L., Xu, W. Y., Deng, Z. Z.,
684   Ma, N., Mildenberger, K., Henning, S., Stratmann, F., and Wiedensohler, A.: Hygroscopic
685   properties of aerosol particles at high relative humidity and their diurnal variations in the
686   North China Plain, Atmospheric Chem. Phys., 11, 3479–3494, https://doi.org/10.5194/acp-
687   11-3479-2011, 2011.

688   Liu, X. and Wang, J.: How important is organic aerosol hygroscopicity to aerosol indirect
689   forcing?, Environ. Res. Lett., 5, 044010, https://doi.org/10.1088/1748-9326/5/4/044010,
690   2010.

691   Magi, B. I. and Hobbs, P. V.: Effects of humidity on aerosols in southern Africa during the
692   biomass burning season, J. Geophys. Res. Atmospheres, 108,
693   https://doi.org/10.1029/2002JD002144, 2003.

694   Mayer, K. J., Wang, X., Santander, M. V., Mitts, B. A., Sauer, J. S., Sultana, C. M., Cappa,
695   C. D., and Prather, K. A.: Secondary Marine Aerosol Plays a Dominant Role over Primary
696   Sea Spray Aerosol in Cloud Formation, ACS Cent. Sci., 6, 2259–2266,
697   https://doi.org/10.1021/acscentsci.0c00793, 2020.

698   Mei, F., Hayes, P. L., Ortega, A., Taylor, J. W., Allan, J. D., Gilman, J., Kuster, W., de
699   Gouw, J., Jimenez, J. L., and Wang, J.: Droplet activation properties of organic aerosols
700   observed at an urban site during CalNex-LA, J. Geophys. Res. Atmospheres, 118, 2903–
701   2917, https://doi.org/10.1002/jgrd.50285, 2013.

702   Mie, G.: Beiträge zur Optik trüber Medien, speziell kolloidaler Metallösungen, Ann. Phys.,
703   330, 377–445, https://doi.org/10.1002/andp.19083300302, 1908.

704   Petters, M. D. and Kreidenweis, S. M.: A single parameter representation of hygroscopic
705   growth and cloud condensation nucleus activity, Atmos Chem Phys, 11, 2007.

706   Petters, M. D., Carrico, C. M., Kreidenweis, S. M., Prenni, A. J., DeMott, P. J., Collett, J. L.,
707   and Moosmüller, H.: Cloud condensation nucleation activity of biomass burning aerosol, J.
708   Geophys. Res., 114, D22205, https://doi.org/10.1029/2009JD012353, 2009.

709   Quinn, P. K., Bates, T. S., Baynard, T., Clarke, A. D., Onasch, T. B., Wang, W., Rood, M. J.,
710   Andrews, E., Allan, J., Carrico, C. M., Coffman, D., and Worsnop, D.: Impact of particulate
711   organic matter on the relative humidity dependence of light scattering: A simplified
712   parameterization, Geophys. Res. Lett., 32, https://doi.org/10.1029/2005GL024322, 2005.

713   Rastak, N., Pajunoja, A., Acosta Navarro, J. C., Ma, J., Song, M., Partridge, D. G., Kirkevåg,
714   A., Leong, Y., Hu, W. W., Taylor, N. F., Lambe, A., Cerully, K., Bougiatioti, A., Liu, P.,
715   Krejci, R., Petäjä, T., Percival, C., Davidovits, P., Worsnop, D. R., Ekman, A. M. L., Nenes,
716   A., Martin, S., Jimenez, J. L., Collins, D. R., Topping, D. o., Bertram, A. K., Zuend, A.,
717   Virtanen, A., and Riipinen, I.: Microphysical explanation of the RH-dependent water affinity
718   of biogenic organic aerosol and its importance for climate, Geophys. Res. Lett., 44, 5167–
719   5177, https://doi.org/10.1002/2017GL073056, 2017.

720   Reddington, C. L., Morgan, W. T., Darbyshire, E., Brito, J., Coe, H., Artaxo, P., Scott, C. E.,
721   Marsham, J., and Spracklen, D. V.: Biomass burning aerosol over the Amazon: analysis of
722   aircraft, surface and satellite observations using a global aerosol model, Atmospheric Chem.
723   Phys., 19, 9125–9152, https://doi.org/10.5194/acp-19-9125-2019, 2019.

724   Redemann, J., Wood, R., Zuidema, P., Doherty, S. J., Luna, B., LeBlanc, S. E., Diamond, M.
725   S., Shinozuka, Y., Chang, I. Y., Ueyama, R., Pfister, L., Ryoo, J.-M., Dobracki, A. N., da
726   Silva, A. M., Longo, K. M., Kacenelenbogen, M. S., Flynn, C. J., Pistone, K., Knox, N. M.,
727   Piketh, S. J., Haywood, J. M., Formenti, P., Mallet, M., Stier, P., Ackerman, A. S., Bauer, S.
728   E., Fridlind, A. M., Carmichael, G. R., Saide, P. E., Ferrada, G. A., Howell, S. G., Freitag, S.,
729   Cairns, B., Holben, B. N., Knobelspiesse, K. D., Tanelli, S., L'Ecuyer, T. S., Dzambo, A. M.,
730   Sy, O. O., McFarquhar, G. M., Poellot, M. R., Gupta, S., O'Brien, J. R., Nenes, A., Kacarab,
731   M., Wong, J. P. S., Small-Griswold, J. D., Thornhill, K. L., Noone, D., Podolske, J. R.,
732   Schmidt, K. S., Pilewskie, P., Chen, H., Cochrane, S. P., Sedlacek, A. J., Lang, T. J., Stith,
733   E., Segal-Rozenhaimer, M., Ferrare, R. A., Burton, S. P., Hostetler, C. A., Diner, D. J.,
734   Seidel, F. C., Platnick, S. E., Myers, J. S., Meyer, K. G., Spangenberg, D. A., Maring, H., and
735   Gao, L.: An overview of the ORACLES (ObseRvations of Aerosols above CLouds and their
736   intEractionS) project: aerosol–cloud–radiation interactions in the southeast Atlantic basin,
737   Atmospheric Chem. Phys., 21, 1507–1563, https://doi.org/10.5194/acp-21-1507-2021, 2021.

738   Rickards, A. M. J., Miles, R. E. H., Davies, J. F., Marshall, F. H., and Reid, J. P.:
739   Measurements of the Sensitivity of Aerosol Hygroscopicity and the κ Parameter to the O/C
740   Ratio, J. Phys. Chem. A, 117, 14120–14131, https://doi.org/10.1021/jp407991n, 2013.

741   Sheridan, P. J., Jefferson, A., and Ogren, J. A.: Spatial variability of submicrometer aerosol
742   radiative properties over the Indian Ocean during INDOEX, J. Geophys. Res. Atmospheres,
743   107, https://doi.org/10.1029/2000JD000166, 2002.

744   Shingler, T., Crosbie, E., Ortega, A., Shiraiwa, M., Zuend, A., Beyersdorf, A., Ziemba, L.,
745   Anderson, B., Thornhill, L., Perring, A. E., Schwarz, J. P., Campazano-Jost, P., Day, D. A.,
746   Jimenez, J. L., Hair, J. W., Mikoviny, T., Wisthaler, A., and Sorooshian, A.: Airborne
747   characterization of subsaturated aerosol hygroscopicity and dry refractive index from the
748   surface to 6.5 km during the SEAC4RS campaign, J. Geophys. Res. Atmospheres, 121,
749   4188–4210, https://doi.org/10.1002/2015JD024498, 2016.

750   Suda, S. R., Petters, M. D., Matsunaga, A., Sullivan, R. C., Ziemann, P. J., and Kreidenweis,
751   S. M.: Hygroscopicity frequency distributions of secondary organic aerosols, J. Geophys.
752   Res. Atmospheres, 117, https://doi.org/10.1029/2011JD016823, 2012.

753   Sumlin, B. J., Heinson, Y. W., Shetty, N., Pandey, A., Pattison, R. S., Baker, S., Hao, W. M.,
754   and Chakrabarty, R. K.: UV–Vis–IR spectral complex refractive indices and optical
755   properties of brown carbon aerosol from biomass burning, J. Quant. Spectrosc. Radiat.
756   Transf., 206, 392–398, https://doi.org/10.1016/j.jqsrt.2017.12.009, 2018.

757 Thompson, G. and Eidhammer, T.: A Study of Aerosol Impacts on Clouds and Precipitation
758 Development in a Large Winter Cyclone, J. Atmospheric Sci., 71, 3636–3658,
759 https://doi.org/10.1175/JAS-D-13-0305.1, 2014.

760 Titos, G., Cazorla, A., Zieger, P., Andrews, E., Lyamani, H., Granados-Muñoz, M. J., Olmo,
761 F. J., and Alados-Arboledas, L.: Effect of hygroscopic growth on the aerosol light-scattering
762 coefficient: A review of measurements, techniques and error sources, Atmos. Environ., 141,
763 494–507, https://doi.org/10.1016/j.atmosenv.2016.07.021, 2016.

764 Titos, G., Burgos, M. A., Zieger, P., Alados-Arboledas, L., Baltensperger, U., Jefferson, A.,
765 Sherman, J., Weingartner, E., Henzing, B., Luoma, K., O'Dowd, C., Wiedensohler, A., and
766 Andrews, E.: A global study of hygroscopicity-driven light-scattering enhancement in the
767 context of other in situ aerosol optical properties, Atmospheric Chem. Phys., 21, 13031–
768 13050, https://doi.org/10.5194/acp-21-13031-2021, 2021.

769 Wang, J., Shilling, J. E., Liu, J., Zelenyuk, A., Bell, D. M., Petters, M. D., Thalman, R., Mei,
770 F., Zaveri, R. A., and Zheng, G.: Cloud droplet activation of secondary organic aerosol is
771 mainly controlled by molecular weight, not water solubility, Atmospheric Chem. Phys., 19,
772 941–954, https://doi.org/10.5194/acp-19-941-2019, 2019.

773 Wang, W., Rood, M. J., Carrico, C. M., Covert, D. S., Quinn, P. K., and Bates, T. S.: Aerosol
774 optical properties along the northeast coast of North America during the New England Air
775 Quality Study–Intercontinental Transport and Chemical Transformation 2004 campaign and
776 the influence of aerosol composition, J. Geophys. Res. Atmospheres, 112,
777 https://doi.org/10.1029/2006JD007579, 2007.

778 van der Werf, G. R., Randerson, J. T., Giglio, L., Collatz, G. J., Mu, M., Kasibhatla, P. S.,
779 Morton, D. C., DeFries, R. S., Jin, Y., and van Leeuwen, T. T.: Global fire emissions and the
780 contribution of deforestation, savanna, forest, agricultural, and peat fires (1997–2009),
781 Atmospheric Chem. Phys., 10, 11707–11735, https://doi.org/10.5194/acp-10-11707-2010,
782 2010.

783 Wu, H., Taylor, J. W., Szpek, K., Langridge, J. M., Williams, P. I., Flynn, M., Allan, J. D.,
784 Abel, S. J., Pitt, J., Cotterell, M. I., Fox, C., Davies, N. W., Haywood, J., and Coe, H.:
785 Vertical variability of the properties of highly aged biomass burning aerosol transported over
786 the southeast Atlantic during CLARIFY-2017, Atmospheric Chem. Phys., 20, 12697–12719,
787 https://doi.org/10.5194/acp-20-12697-2020, 2020.

788 Zhang, L., Sun, J. Y., Shen, X. J., Zhang, Y. M., Che, H., Ma, Q. L., Zhang, Y. W., Zhang, X.
789 Y., and Ogren, J. A.: Observations of relative humidity effects on aerosol light scattering in
790 the Yangtze River Delta of China, Atmospheric Chem. Phys., 15, 8439–8454,
791 https://doi.org/10.5194/acp-15-8439-2015, 2015a.

792 Zhang, L., Sun, J. Y., Shen, X. J., Zhang, Y. M., Che, H., Ma, Q. L., Zhang, Y. W., Zhang, X.
793 Y., and Ogren, J. A.: Observations of relative humidity effects on aerosol light scattering in
794 the Yangtze River Delta of China, Atmospheric Chem. Phys., 15, 8439–8454,
795 https://doi.org/10.5194/acp-15-8439-2015, 2015b.

796 Zhang, L., Segal-Rozenhaimer, M., Che, H., Dang, C., Sedlacek III, A. J., Lewis, E. R.,
797 Dobracki, A., Wong, J. P. S., Formenti, P., Howell, S. G., and Nenes, A.: Light absorption by

798   brown carbon over the South-East Atlantic Ocean, Atmospheric Chem. Phys., 22, 9199–
799   9213, https://doi.org/10.5194/acp-22-9199-2022, 2022.

800   Zhang, Q., Jimenez, J. L., Canagaratna, M. R., Allan, J. D., Coe, H., Ulbrich, I., Alfarra, M.
801   R., Takami, A., Middlebrook, A. M., Sun, Y. L., Dzepina, K., Dunlea, E., Docherty, K.,
802   DeCarlo, P. F., Salcedo, D., Onasch, T., Jayne, J. T., Miyoshi, T., Shimono, A., Hatakeyama,
803   S., Takegawa, N., Kondo, Y., Schneider, J., Drewnick, F., Borrmann, S., Weimer, S.,
804   Demerjian, K., Williams, P., Bower, K., Bahreini, R., Cottrell, L., Griffin, R. J., Rautiainen,
805   J., Sun, J. Y., Zhang, Y. M., and Worsnop, D. R.: Ubiquity and dominance of oxygenated
806   species in organic aerosols in anthropogenically-influenced Northern Hemisphere
807   midlatitudes, Geophys. Res. Lett., 34, https://doi.org/10.1029/2007GL029979, 2007.

808   Zieger, P., Fierz-Schmidhauser, R., Gysel, M., Ström, J., Henne, S., Yttri, K. E.,
809   Baltensperger, U., and Weingartner, E.: Effects of relative humidity on aerosol light
810   scattering in the Arctic, Atmospheric Chem. Phys., 10, 3875–3890,
811   https://doi.org/10.5194/acp-10-3875-2010, 2010.

812   Zieger, P., Fierz-Schmidhauser, R., Weingartner, E., and Baltensperger, U.: Effects of
813   relative humidity on aerosol light scattering: results from different European sites,
814   Atmospheric Chem. Phys., 13, 10609–10631, https://doi.org/10.5194/acp-13-10609-2013,
815   2013.

816   Zieger, P., Fierz-Schmidhauser, R., Poulain, L., Müller, T., Birmili, W., Spindler, G.,
817   Wiedensohler, A., Baltensperger, U., and Weingartner, E.: Influence of water uptake on the
818   aerosol particle light scattering coefficients of the Central European aerosol, Tellus B Chem.
819   Phys. Meteorol., 66, 22716, https://doi.org/10.3402/tellusb.v66.22716, 2014.

820   Zieger, P., Aalto, P. P., Aaltonen, V., Äijälä, M., Backman, J., Hong, J., Komppula, M.,
821   Krejci, R., Laborde, M., Lampilahti, J., de Leeuw, G., Pfüller, A., Rosati, B., Tesche, M.,
822   Tunved, P., Väänänen, R., and Petäjä, T.: Low hygroscopic scattering enhancement of boreal
823   aerosol and the implications for a columnar optical closure study, Atmospheric Chem. Phys.,
824   15, 7247–7267, https://doi.org/10.5194/acp-15-7247-2015, 2015.

825